# Supporting Information for "Ship aerosol emissions and marine fuel regulations: Impacts on physicochemical properties, cloud activity and emission factors"

L. F. E. d. Santos[1], K. Salo[2], X. Kong[1], M. Hartmann[1] *, J. Sjöblom[3], and

Erik S. Thomson[1]

[1]Department of Chemistry and Molecular Biology, Atmospheric Science, University of Gothenburg, Gothenburg, Sweden

[2]Department of Mechanics and Maritime Sciences, Maritime Studies, Chalmers University of Technology, Gothenburg, Sweden

[3]Department of Mechanics and Maritime Sciences, Combustion and Propulsion Systems, Chalmers University of Technology, Gothenburg, Sweden

## Contents of this file

1. Figures S1 to S18

## Introduction

*Current address, Department for Atmospheric Microphysics, Leibniz Institute for Tropospheric Research, Leipzig, Germany

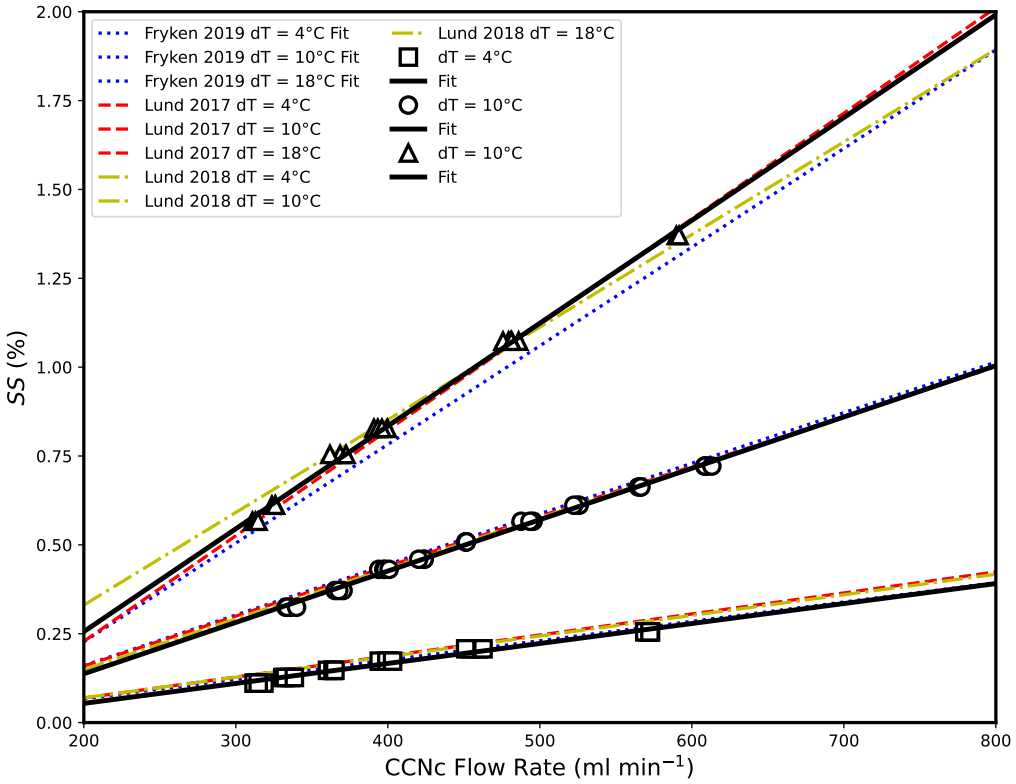


**Figure S1.** Calibration results of the CCNc instrument performed with ammonium sulfate ($(NH_4)_2SO_4$) at $\Delta T$=4 K, 10 K and 18 K. Least-squares linear fits (solid black lines) were performed on the measured data (markers) to determine the sample flow dependent supersaturation within the instrument. The results are compared to previous calibrations performed with the same instrument.

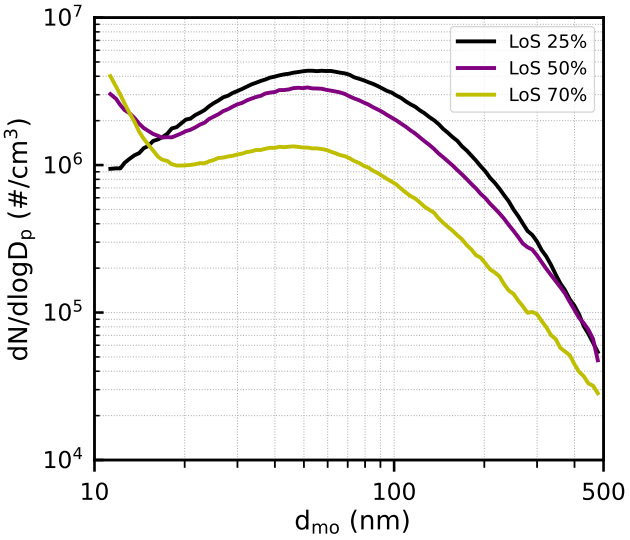


**Figure S2.** Average LoS particle size distributions reproduced from Figure 2a-c.

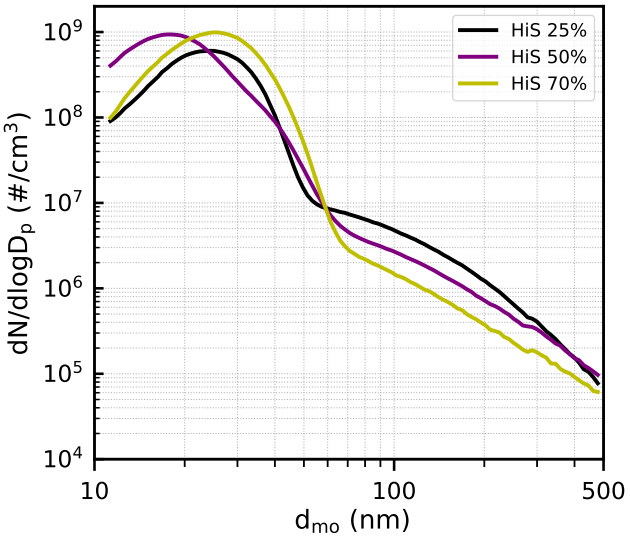


**Figure S3.** Average HiS particle size distributions reproduced from Figure 2a-c.

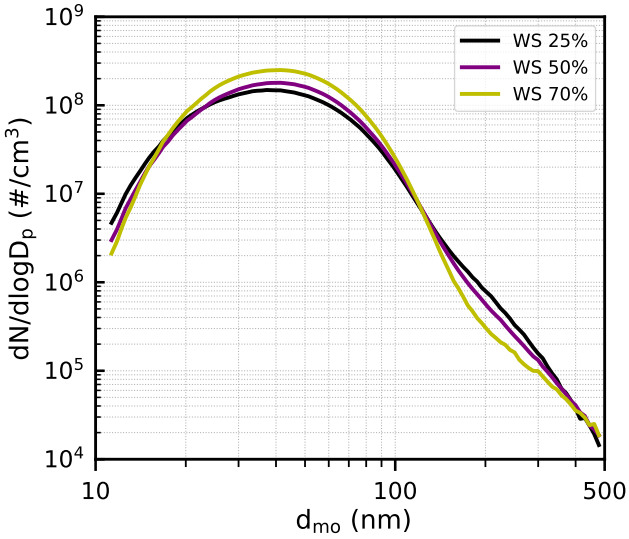


**Figure S4.** Average WS particle size distributions reproduced from Figure 2a-c.

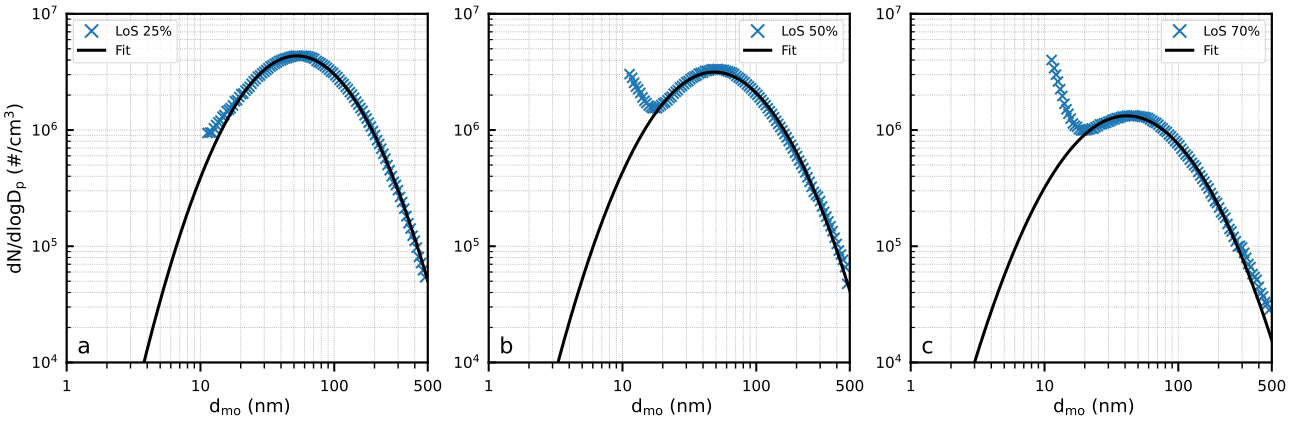


**Figure S5.** (a - c) Unimodal lognormal least-squares fitting of mean particle size distributions (PSDs) for all LoS load cases. The average PSDs are replotted from Figure 2a-c. During the fitting process, SMPS size-bins below 20 nm were ignored due to large variability of particle concentrations within the smallest size bins.

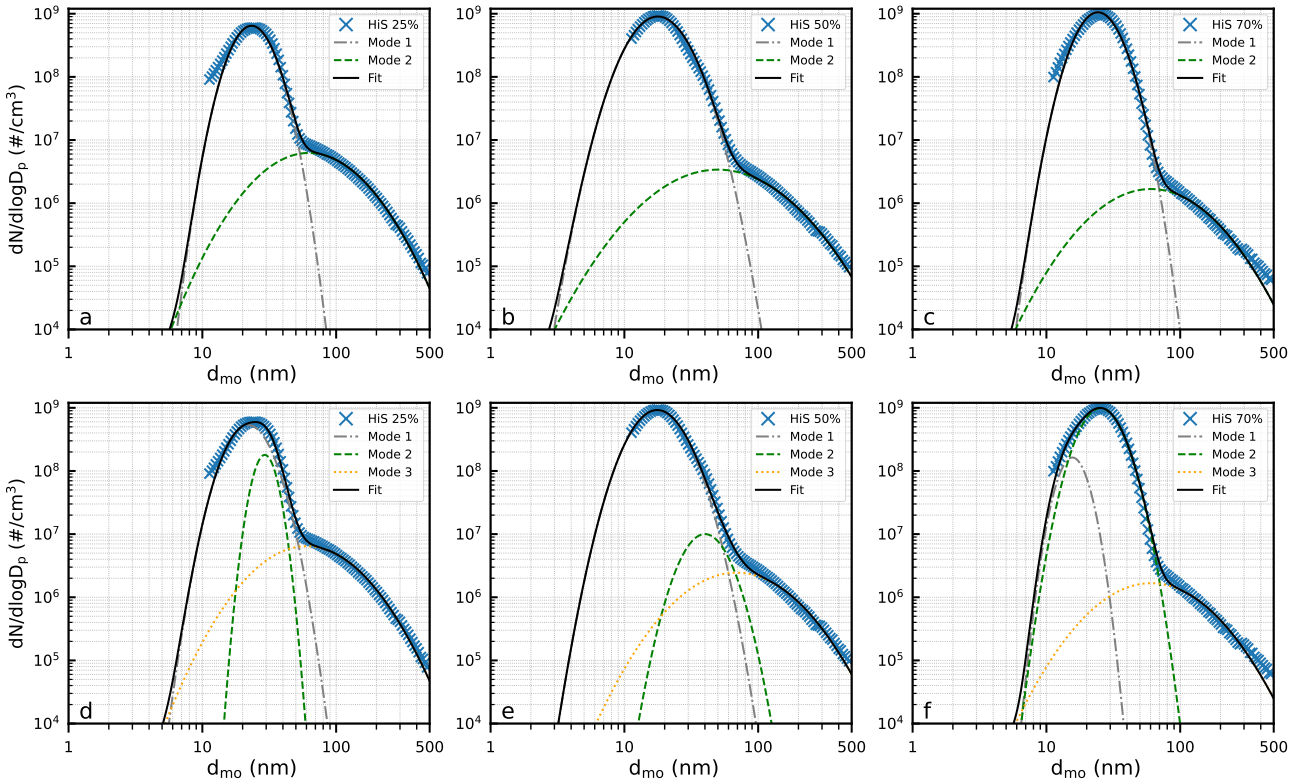


**Figure S6.** (a - c) Bimodal and (d - f) trimodal lognormal least-squares fitting of mean particle size distributions (PSDs) for all HiS load cases. The average PSDs are replotted from Figure 2a-c.

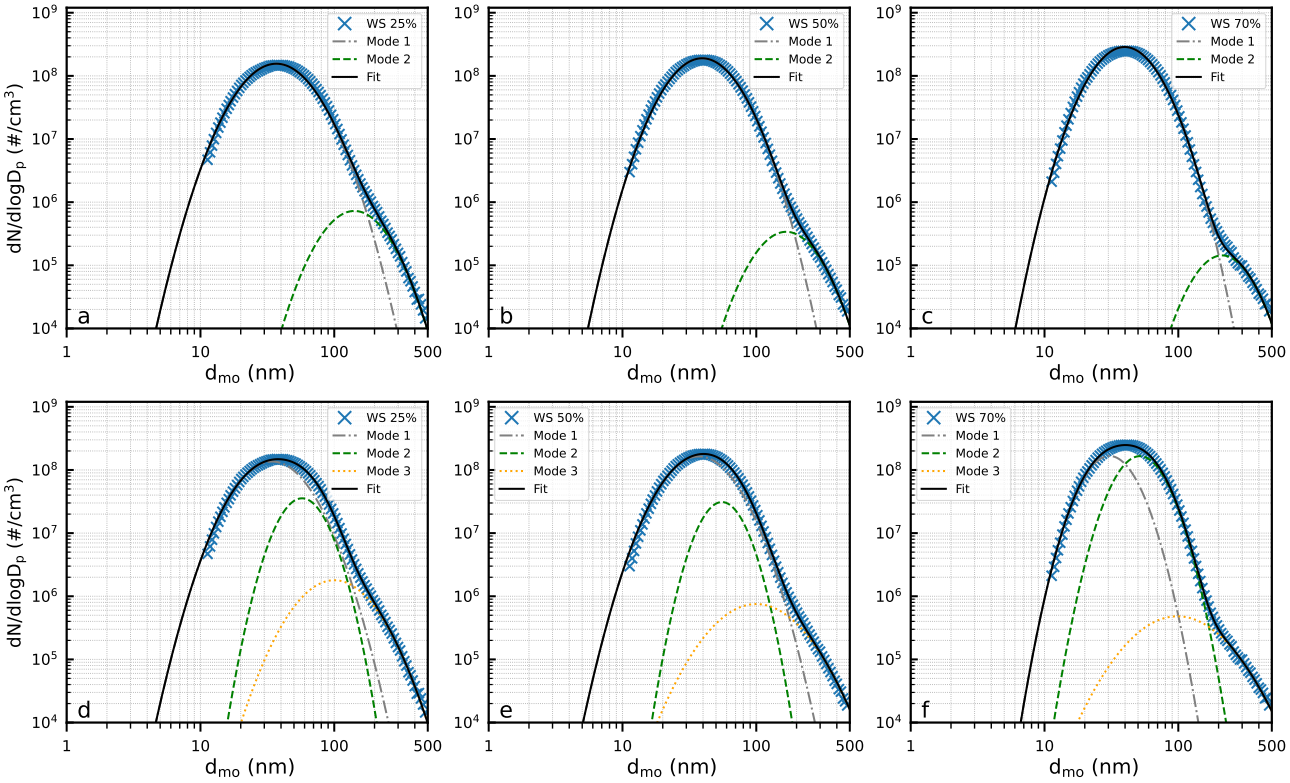


**Figure S7.** (a - c) Bimodal and (d - f) trimodal lognormal least-squares fitting of mean particle size distributions (PSDs) for all WS load cases. The average PSDs are replotted from Figure 2a-c.

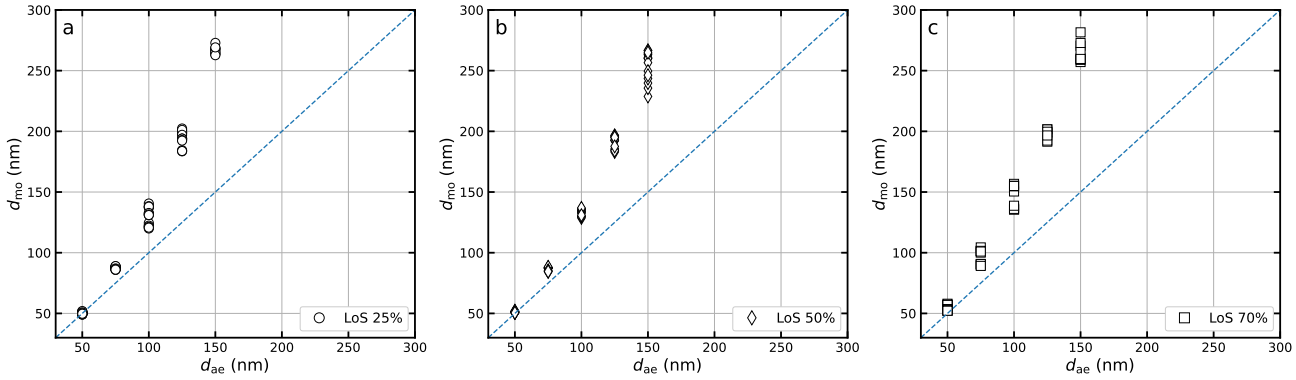


**Figure S8.** Raw data output of combined AAC and SMPS measurements of size-selected LoS exhaust particles. The aerodynamic diameters ($d_{ae}$) result from size-selection using the AAC, whereas the corresponding mobility diameters ($d_{mo}$) are derived from normal distributions fitted to the size distributions measured with the SMPS downstream of the AAC. Data is shown for engine loads of (a) 25%, (b) 50% and (c) 75%.

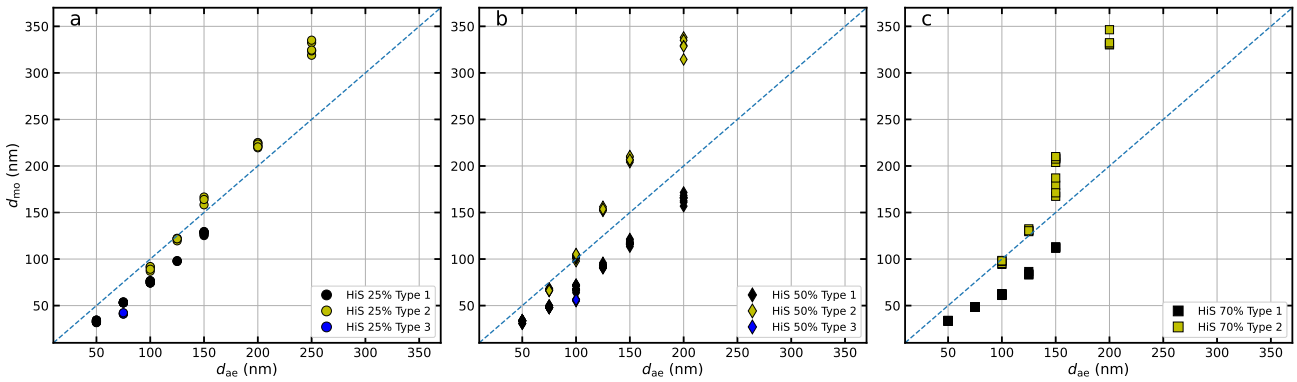


**Figure S9.** Raw data output of combined AAC and SMPS measurements of size-selected HiS exhaust particles. The aerodynamic diameters ($d_{ae}$) result from size-selection using the AAC, whereas the corresponding mobility diameters ($d_{mo}$) are derived from normal distributions fitted to the size distributions measured with the SMPS downstream of the AAC. Data is shown for engine loads of (a) 25%, (b) 50% and (c) 75%. Classification into different particle types was estimated based on observed trends in the data distribution.

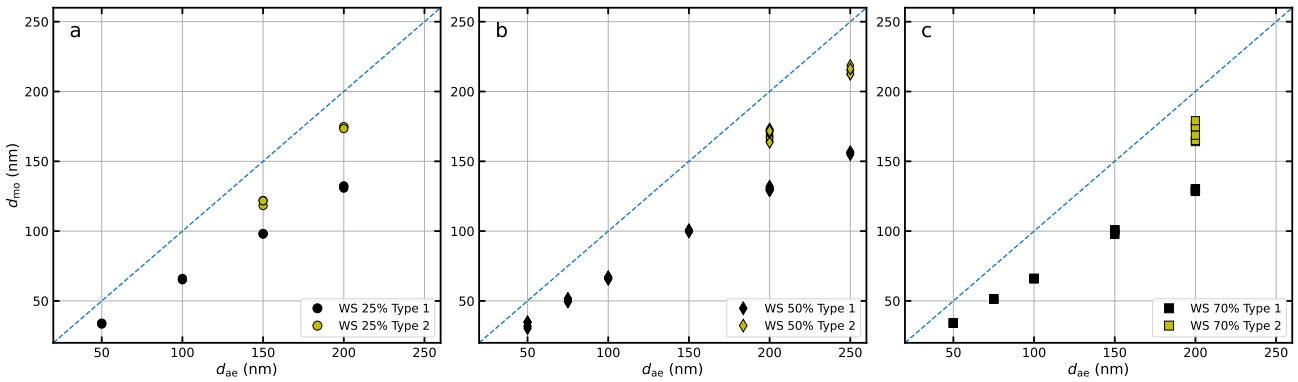


**Figure S10.** Raw data output of combined AAC and SMPS measurements of size-selected WS exhaust particles. The aerodynamic diameters ($d_{ae}$) result from size-selection using the AAC, whereas the corresponding mobility diameters ($d_{mo}$) are derived from normal distributions fitted to the size distributions measured with the SMPS downstream of the AAC. Data is shown for engine loads of (a) 25%, (b) 50% and (c) 75%. Classification into different particle types was estimated based on observed trends in the data distribution.

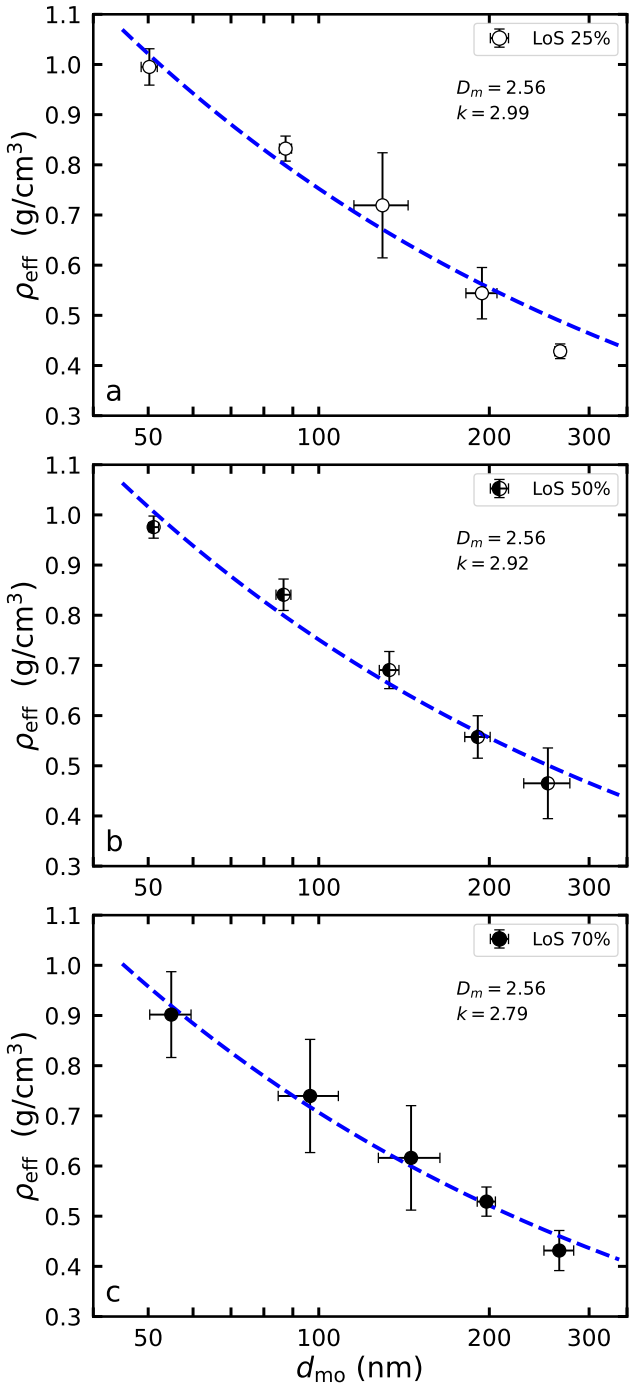


**Figure S11.** Effective densities ($\rho_{\text{eff}}$) determined for LoS exhaust particles at different engine loads, i.e. (a) 25%, (b) 50% and (c) 75%. The dashed blue line shows the mass-mobility power law fitting. The corresponding fitting parameters, i.e. the fractal dimensions ($D_m$) and constants ($k$), are given below the legends. The error bars depict ± two standard deviations.

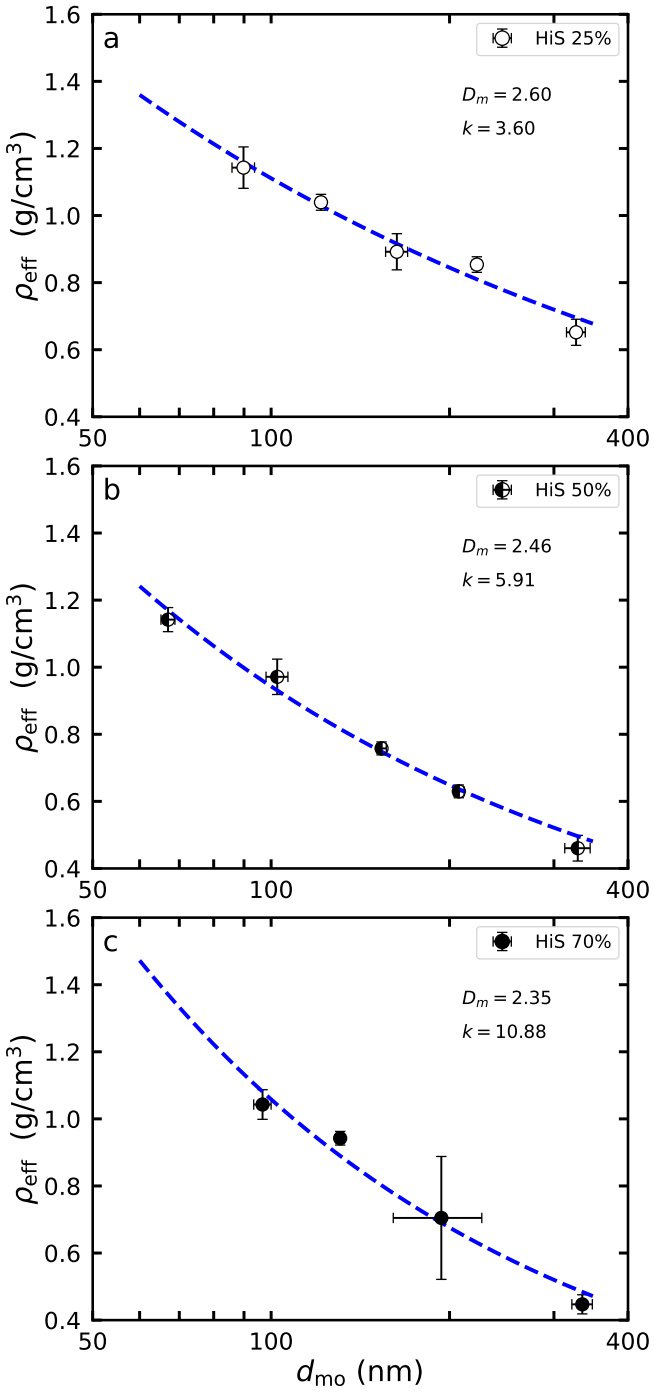


**Figure S12.** Effective densities ($\rho_{\text{eff}}$) determined for Type 2 HiS exhaust particles at different engine loads, i.e. (a) 25%, (b) 50% and (c) 75%. The dashed blue line shows the mass-mobility power law fitting. The corresponding fitting parameters, i.e. the fractal dimensions ($D_m$) and constants ($k$), are given below the legends. The error bars depict ± two standard deviations.

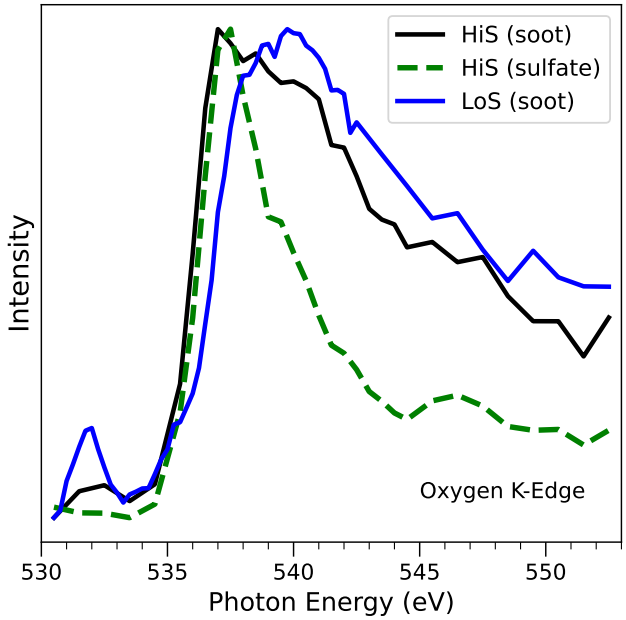


**Figure S13.** Comparison between NEXAFS oxygen K-Edge spectra of the LoS soot particle (replotted from Figure 4) and the HiS soot and sulfate particles (replotted from Figure 5).

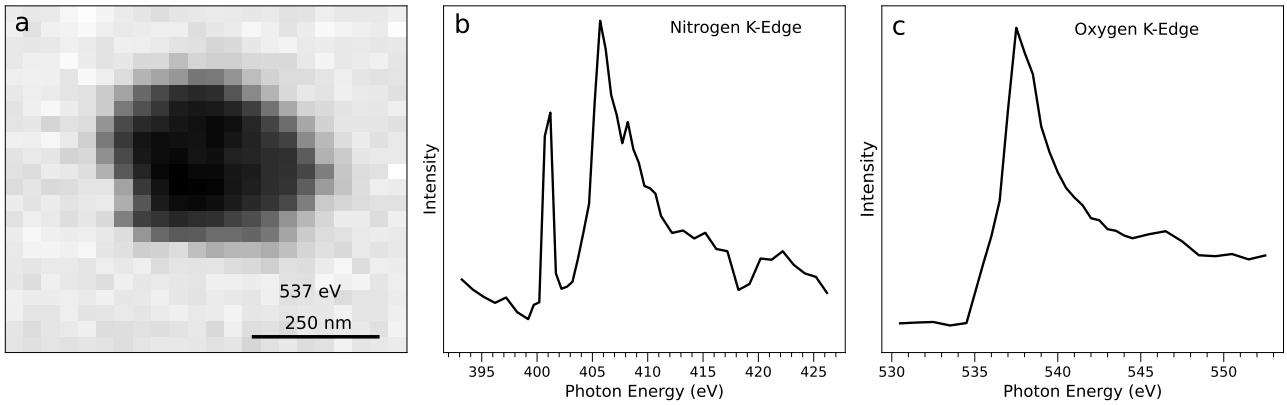


**Figure S14.** (a) STXM image of a WS sulfate particle. NEXAFS spectra at (b) the nitrogen K-Edge and (c) the oxygen K-Edge.

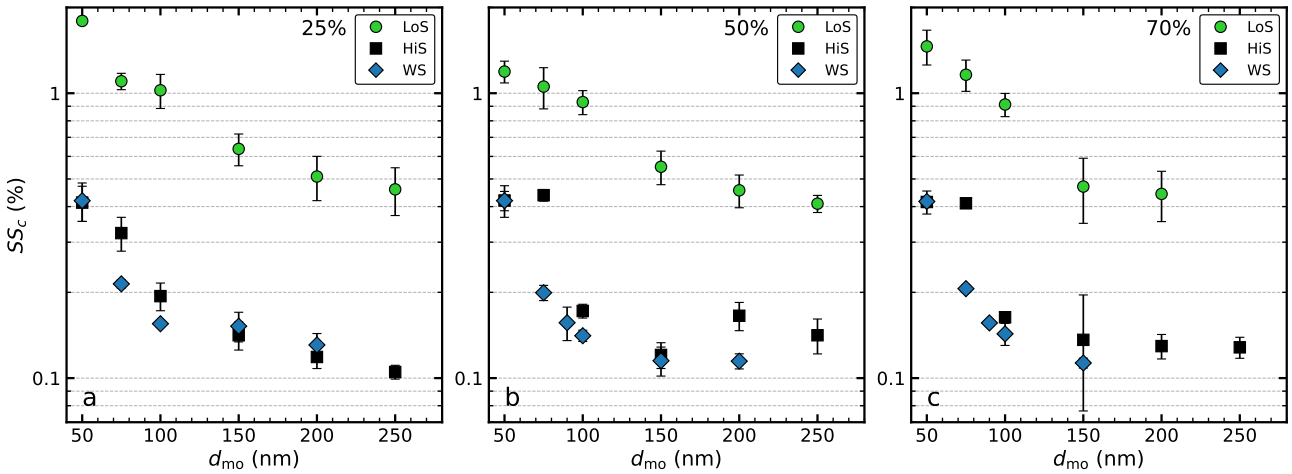


**Figure S15.** Critical supersaturations ($SS_c$) measured with the CCNc for size-selected LoS, HiS and WS particles. Individual panels show results for engine loads of (a) 25%, (b) 50% and (c) 75%.

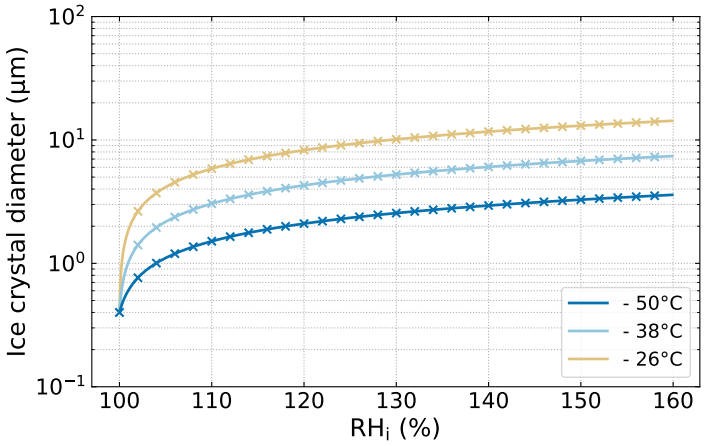


**Figure S16.** Ice crystal growth model results for a residence time of 15 s (typical for PINCii) and an initial seed particle diameter of 200 nm.

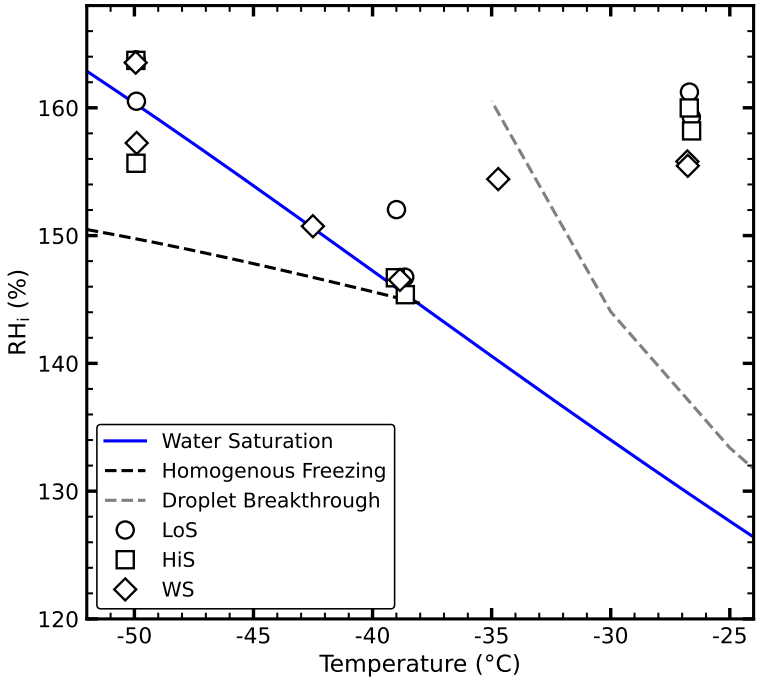


**Figure S17.** Ice nucleation results derived from an alternative approach, where the freezing onsets (1% of activated fraction) are plotted as function of average lamina temperature and maximum occurring $RH_i$.

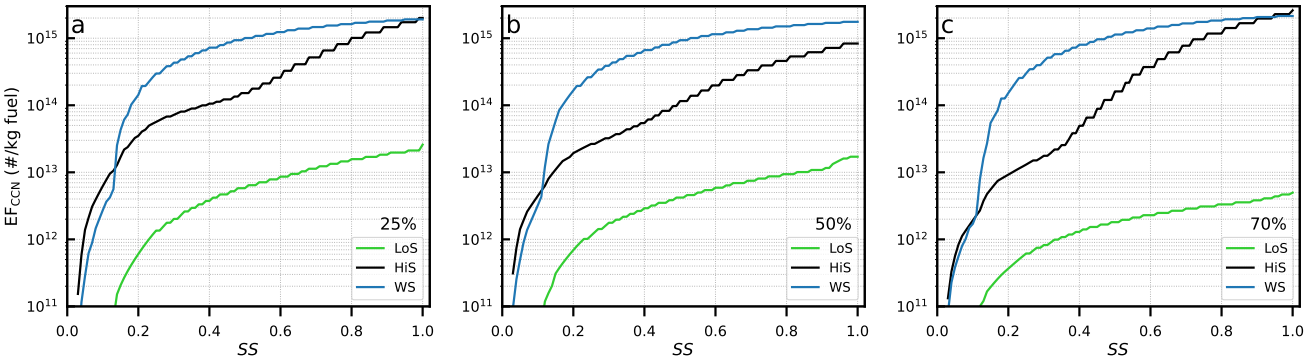


**Figure S18.** CCN emission factors ($EF_{CCN}$) derived from interpolated $\kappa$ values as a function of supersaturation ($SS$). The panels show results for engine loads of (a) 25%, (b) 50% and (c) 70%.